Supplementary information for: Defect engineering in plasmonic metal oxide nanocrystals

Evan L. Runnerstrom, Amy Bergerud, Ankit Agrawal, Robert W. Johns, Clayton J. Dahlman, Ajay Singh, Sverre M. Selbach, Delia J. Milliron*
* To whom correspondence should be addressed. Email: milliron@che.utexas.edu

Section S1: Synthetic procedures

Materials: All chemicals were used as received without further purification. Indium acetylacetonate (In-acac, 99.99%), cerium (III) acetylacetonate hydrate (Ce-acac), cerium (III) acetate hydrate (Ce-acetate), cerium (IV) ammonium nitrate (C.A.N., 98.5%) and tin bis(acetylacetonate) dichloride ($Sn(acac)_2Cl_2$ 98 %) were purchased from Sigma Aldrich. Cerium (IV) tetramethylheptanedionate (Ce-TMHD, 97%) and cerium (III) acetate (Ce-acetate, 99.9%) were purchased from Strem. Oleylamine (OLAM, 80-90%) was obtained from Acros Organics.

Methods: All nanocrystals were synthesized using slight modifications of literature procedures. All synthetic procedures were carried out under inert nitrogen atmosphere with magnetic stirring using standard Schlenk line techniques and 50 mL three-neck round bottom flasks.

For all syntheses, the molar ratio of metal precursor to OLAM was set at 1:12. Doping was achieved by adding the desired cerium and/or tin precursor while maintaining the total metal:OLAM ratio. For example, to synthesize 5.2% Ce-doped In_2O_3 nanocrystals, 0.85 mmol In-acac (350 mg) was combined with 0.045 mmol Ce-acac (20 mg) and 11 mmol OLAM (2.934 g). The solution was heated to 110°C for 10 minutes under nitrogen, then heated to 250°C for 2 hours. The nanocrystals in the crude reaction mixture were purified by three cycles of flocculation with ethanol, centrifugation, and redispersion in hexanes before finally being dispersed in hexanes and filtered with a syringe filter.

Section S2: Sample characterization

Transmission electron microscopy (TEM) was used to characterize size and shape of the synthesized nanocrystals. TEM samples were prepared by diluting 10 microliters of the purified nanocrystal dispersion into 1 mL of toluene before dropcasting 10 microliters of the diluted toluene dispersion onto a copper TEM grid. TEM micrographs were collected using a JEOL 2010F TEM, with a Schottky field emission source, operated at 200 kV accelerating voltage. Low-resolution scanning TEM (STEM) micrographs were obtained using a Hitachi S5500 scanning electron microscope operating in STEM mode at 30 kV accelerating voltage.

X-ray diffraction (XRD) was used to confirm the crystalline phase of the as-synthesized nanocrystal samples dropcast onto silicon. XRD powder diffraction patterns were collected using a Rigaku MiniFlex 600 with a Cu Kα x-ray source and a point detector, operating in Bragg-Bretano geometry. Rietveld refinement was performed using the TOPAS program.

XRD patterns were fit to the bixbyite crystal structure (space group Ia-3), refining lattice parameter, sample displacement, peak profile, scale, and background function.

Optical spectra of the nanocrystal dispersions were collected in an FTIR liquid cell to characterize their LSPR properties. Because most organic solvents have strong molecular vibrations (e.g., C-H stretch) that would interfere with FTIR measurements, we precipitated the nanocrystals out of hexane and redispersed them in a desired solvent for IR spectroscopy, such as tetrachloroethylene, taking care to remove as much hexane and ethanol as possible. The tetrachloroethylene nanocrystal dispersions were injected via syringe into a liquid cell with IR transparent KBr windows, with a pathlength of 0.5 mm, for FTIR spectroscopy. The collected spectra (in tetrachloroethylene) are shown in Figure S3 along with the Drude model fits.

The optical band gaps of the nanocrystals dispersed in hexanes were measured using 1 cm path length quartz cuvette and an Agilent Cary 5000 spectrophotometer.

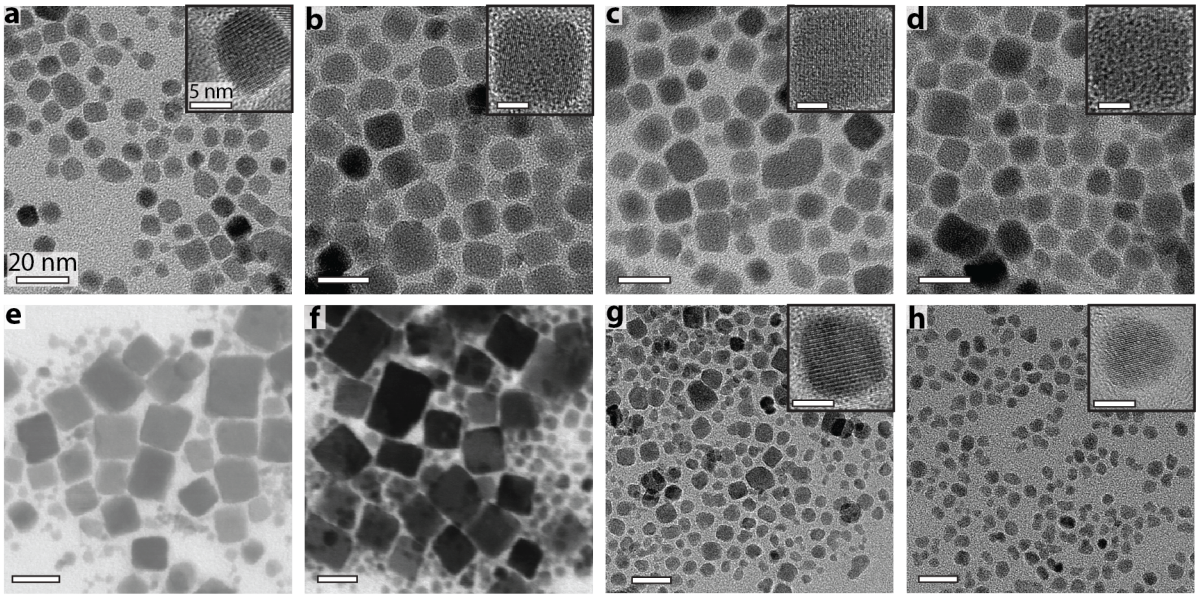

Figure S1: TEM images (high resolution images in insets) of Ce:In_2O_3 nanocrystals. The cerium precursors used were Ce-acac (a-f), Ce-acetate (g) and C.A.N. Panels (e) and (f) are low-resolution STEM images. Ce doping levels: (a) 0.9%; (b) 2.0%; (c) 3.5%; (d) 3.7%; (e) 8.6%; (f) 11.1%; (g) 4.8%; (h) 5.6%. All scale bars are 20 nm, 5 nm for inset images.

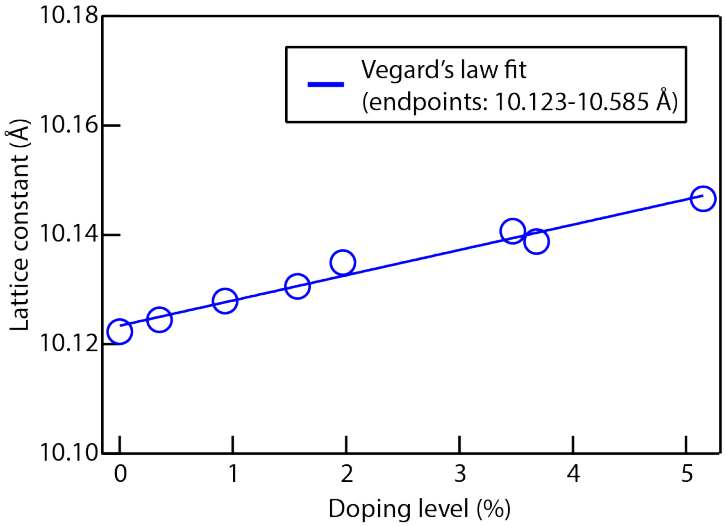

Figure S2: Lattice constant of Ce:In_2O_3 nanocrystals as calculated from Rietveld refinement of powder XRD patterns. The solid line is a fit of Vegard's law to the change in lattice parameter with doping level. The endpoints of the fit (i.e., 0% Ce extrapolated to 100% Ce) are listed in the legend.

Section S3: Drude Modeling

The Drude model can be used to fit optical LSPR spectra and extract quantitative information about the optoelectronic properties of the nanocrystals under study. A material's optical response depends on its frequency dependent dielectric function; for an isolated, conductive nanocrystal, this is primarily the Drude contribution:

$$\varepsilon_{\text{particle}}(\omega) = \varepsilon_{\infty} - \frac{\omega_p^2}{\omega^2 + i\omega\Gamma(\omega)}$$

where ε_{∞} is the high frequency permittivity of the material, Γ is a frequency-dependent electronic damping function, and ω_p is the bulk plasma frequency, given by:

$$\omega_p = \sqrt{\frac{ne^2}{\varepsilon_0 m^*}}$$

where n is the free electron concentration, e is the charge of an electron, m^* is the electron effective mass, and ε_0 is the permittivity of vacuum. The frequency-dependent damping component Γ is given by the empirical function:

$$\Gamma(\omega) = \Gamma_{\text{L}} - \frac{\Gamma_{\text{L}} - \Gamma_{\text{H}}}{\pi}\left[\tan^{-1}\left(\frac{\omega - \Gamma_{\text{X}}}{\Gamma_{\text{W}}}\right) + \frac{\pi}{2}\right]$$

where Γ_{L} is a low-frequency damping constant, Γ_{H} is a high-frequency damping constant, Γ_{X} is a crossover frequency between the low-frequency and high-frequency damping regimes, and Γ_{W} is the width of the crossover region.

Because the nanocrystals are dispersed in solvent at appreciable concentrations for the liquid cell FTIR measurements, we employ the Maxwell-Garnett effective medium approximation (EMA) to account for far-field interactions between nanocrystals and for dielectric interactions between the nanocrystals and the solvent. The EMA is:

$$\frac{\varepsilon_{\text{effective}} - \varepsilon_{\text{solvent}}}{\varepsilon_{\text{effective}} + 2\varepsilon_{\text{solvent}}} = f_v\left(\frac{\varepsilon_{\text{particle}} - \varepsilon_{\text{solvent}}}{\varepsilon_{\text{particle}} + 2\varepsilon_{\text{solvent}}}\right)$$

where $\varepsilon_{\text{effective}}$ is the effective dielectric function of the nanocrystal-solvent dispersion, $\varepsilon_{\text{solvent}}$ is the dielectic constant of the dispersing solvent, $\varepsilon_{\text{particle}}$ is the dielectric function of an isolated nanocrystal in vacuum (see above), and f_v is the volume fraction of nanocrystals dispersed in the solvent. Once $\varepsilon_{\text{effective}}$ is determined, it can be used to calculate the absorption of the nanocrystal dispersion.

Our MATLAB code combines the above four equations to perform a least-squares fit to the collected spectra and extract the free parameters f_v, ω_{p}, Γ_{L}, Γ_{H}, Γ_{X}, and Γ_{W}. We performed multiple fits to each spectrum using different initial guesses to confirm that the solver converged to the same values. Using an effective mass of $0.4m_e$ (the effective mass of Sn:In_2O_3), the electron concentration and the optically-derived DC mobility can be further determined.

Doping level (by ICP)	ω_p (cm^{-1})	Γ_{L} (cm^{-1})	Γ_{H} (cm^{-1})	Γ_{X} (cm^{-1})	Γ_{W} (cm^{-1})	n (cm^{-3})	μ_{opt} ($cm^2V^{-1}s^{-1}$)
0.9% Ce (acac)	5798 ± 5	1153 ± 12	422 ± 25	3425 ± 31	267 ± 46	$1.50x10^{20}$	20.5
2.0% Ce (acac)	6993 ± 0	867 ± 4	423 ± 8	3145 ± 11	141 ± 16	$2.19 x10^{20}$	26.7
3.5% Ce (acac)	7416 ± 1	764 ± 3	421 ± 6	3261 ± 16	263 ± 17	$2.46 x10^{20}$	30.9
3.7% Ce (acac)	7299 ± 1	795 ± 3	417 ± 7	3242 ± 15	232 ± 16	$2.38 x10^{20}$	29.7
5.2% Ce (acac)	7362 ± 1	715 ± 2	468 ± 7	3679 ± 16	71 ± 12	$2.42 x10^{20}$	32.7
8.6% Ce (acac)	7247 ± 2	1016 ± 3	625 ± 8	3886 ± 9	25 ± 6	$2.35 x10^{20}$	23.0
11.1% Ce (acac)	7433 ± 2	1049 ± 3	594 ± 8	3735 ± 9	49 ± 7	$2.47 x10^{20}$	22.3
6.4% Ce (Ce-TMHD)	7464 ± 3	1216 ± 7	617 ± 10	3581 ± 15	305 ± 27	$2.49 x10^{20}$	19.4
4.8% Ce (Ce-acetate)	7322 ± 4	1059 ± 19	414 ± 26	3469 ± 39	492 ± 80	$2.40 x10^{20}$	22.6
5.6% Ce (C.A.N.)	7561	2900	10	2519	1693	$2.56 x10^{20}$	9.9
1.2% Sn	7190 ± 3	1692 ± 7	920 ± 15	3844 ± 27	361 ± 30	$2.31 x10^{20}$	14.0
2.1% Sn	9300 ± 2	1407 ± 3	991 ± 8	4247 ± 25	184 ± 18	$3.87 x10^{20}$	16.7
4% Sn (approx.)	12997 ± 2	1935 ± 144	0	6030 ± 610	2009 ± 558	$7.55x10^{20}$	13.4
5.3% Ce + 1.0% Sn	8121 ± 3	1050 ± 5	685 ± 14	3794 ± 34	121 ± 25	$2.95x10^{20}$	22.3
5.2% Ce + 2.1% Sn	8722 ± 2	1426 ± 7	972 ± 7	3463 ± 16	226 ± 27	$3.44x10^{20}$	16.4

Table S1: Extended Drude model fitting results. Reliable uncertainties could not be calculated for the 5.6% Ce (C.A.N.) sample.

We also fit the FTIR spectra using a simple Drude model utilizing a frequency-independent (i.e., scalar) damping term γ, in which case equation 1 in the main text becomes:

$$\varepsilon(\omega) = \varepsilon_{\infty} - \frac{\omega_p^2}{\omega^2 + i\omega\gamma}$$

and the optical mobility is calculated from the relations:

$$\sigma = en\mu_{\text{opt}} = \frac{ne^2}{m^*\gamma}$$

Doping level (by ICP)	ω_p (cm^{-1})	γ (cm^{-1})	n (cm^{-3})	μ_{opt} ($cm^2V^{-1}s^{-1}$)
0.9% Ce	5814	1015	1.51×10^{20}	22.9
2.0% Ce	6983	777	2.18×10^{20}	30.1
3.5% Ce	7410	691	2.45×10^{20}	33.7
3.7% Ce	7290	716	2.38×10^{20}	32.5
5.2% Ce	7359	696	2.42×10^{20}	33.6
8.6% Ce	7400	979	2.33×10^{20}	23.9
11.1% Ce	7226	968	2.45×10^{20}	23.6
6.4% Ce (Ce-TMHD)	7425	1072	2.46×10^{20}	21.8
4.8% Ce (Ce-acetate)	7294	884	2.38×10^{20}	26.4
5.6% Ce (C.A.N.)	7550	1232	2.55×10^{20}	18.9
1.2% Sn	7175	1507	2.30×10^{20}	15.4
2.1% Sn	9282	1325	3.85×10^{20}	17.7
4% Sn (approx.)	13009	1355	7.56×10^{20}	17.2
5.3% Ce + 1.0% Sn	8107	990	2.94×10^{20}	23.6
5.2% Ce + 2.1% Sn	8774	1239	3.44×10^{20}	18.8

Table S2: Simple Drude model fitting results

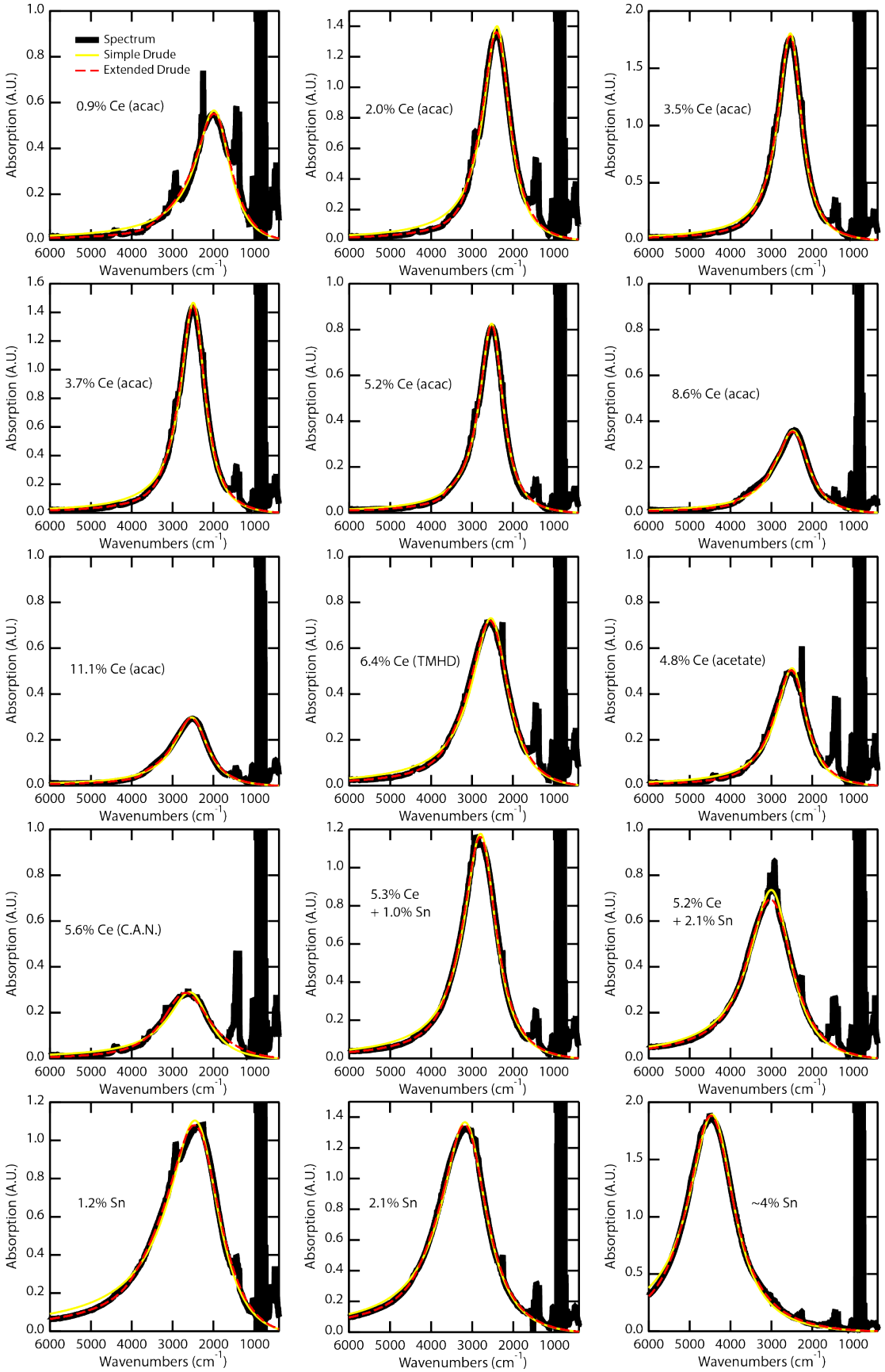

Figure S3: Liquid cell FTIR spectra of the nanocrystals used in this study along with simple Drude and extended Drude optical fits.

Section S4: X-ray absorption spectroscopy (XAS)

Synchrotron X-ray absorption spectra at the Ce $M_{4,5}$-edge we collected at beam line (BL) 8.0.1 and 6.3.2 at the Advanced Light Source (ALS), Lawrence Berkeley National Laboratory, Berkeley, CA. Samples were prepared either by dropcasting hexane dispersions of the nanocrystals onto doped silicon substrates, or by spincasting concentrated nanocrystal dispersions in 1:1 hexane octane. In general, the dropcasted samples gave better total fluorescence yield (TFY), and the spincasted samples gave better total electron yield (TEY). Analysis of Ce oxidation state was performed using TEY spectra. The pre-edge signal was background subtracted using the software from ALS BL 10.3.2 with an edge + elastic fitting algorithm with a quadratic function tailored to the Ce M_5 edge. The spectra were all normalized to the post-edge step background.

The Ce $M_{4,5}$-edge has complex multiplet structure that changes with oxidation state. The reference spectra displayed in Figure S4b show the qualitative differences between Ce^{3+} and Ce^{4+}, and comparison with the Ce:In_2O_3 spectra indicates that a significant portion of Ce dopants in the nanocrystals is in the Ce^{3+} oxidation state. The first three peaks in both the M_5 and M_4 edges (at approximately 879, 882, 883 eV, and 897, 898.5, 900 eV, respectively) are associated with the 3+ oxidation state, while the fourth and fifth peaks in both edges (884, 888.5 eV, and 902, 907 eV) are associated with the 4+ oxidation state. Dividing the areas of all four peaks associated with Ce^{4+} by the sum of the areas of all 10 peaks in the $M_{4,5}$-edge gives the approximate fraction of Ce^{4+} relative to the total Ce content. Multi peak fitting was performed using IGOR Pro software. While the accuracy of this method can be increased by accounting for local Ce coordination environments, we did not perform those corrections for the purpose of this analysis.

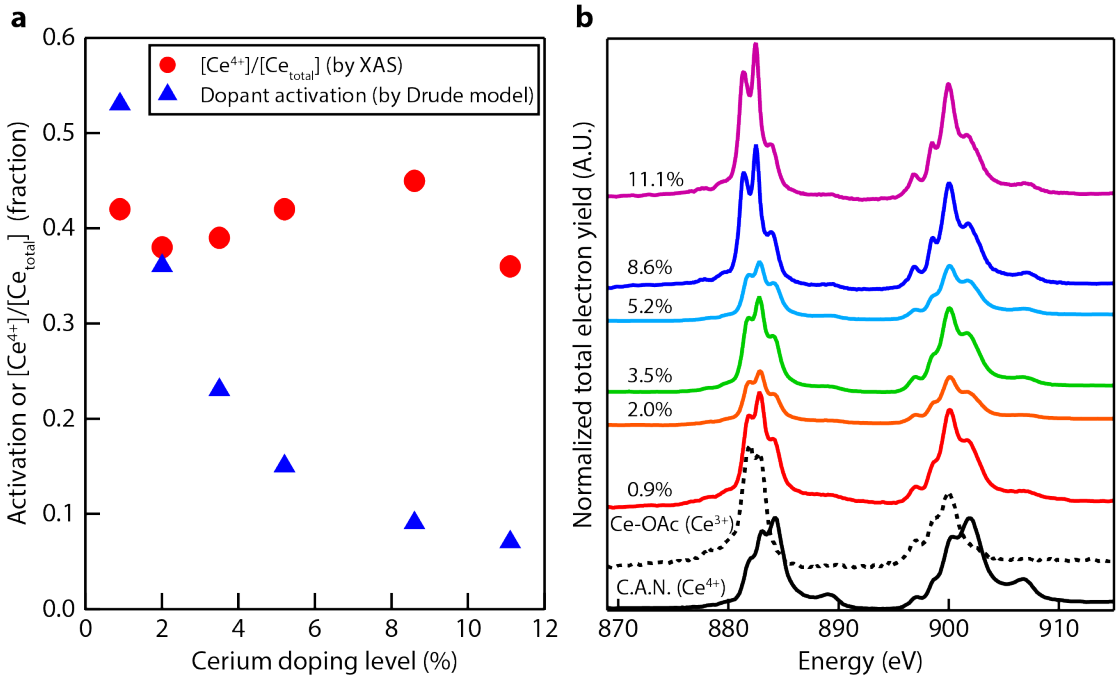

Figure S4: (a) Fraction of activated dopants (blue triangles, calculated as the free electron concentration divided by dopant concentration) in Ce:In_2O_3 nanocrystals, and the fraction of ionized Ce^{4+} in the nanocrystals, calculated by XAS (red circles). (b) XAS spectra of

Ce:In_2O_3 nanocrystals at various doping levels, along with Ce^{4+} and Ce^{3+} reference compounds.

Section S5: DFT simulations

Density Functional Theory: DFT[1,2] calculations were performed using the Vienna *Ab initio* Simulation Package (VASP) with a plane-wave basis set expanded up to a cutoff energy of 550 eV.[3,4] Projector augmented wave (PAW) potentials were used, treating 13 valence electrons for indium ($4d^{10}5s^25p^1$), 14 for tin ($4d^{10}5s^25p^2$), 12 for cerium ($5s^25p^64f^15d^16s^2$), and 6 for oxygen ($2s^22p^4$).[5,6] Brillouin zone integration was done on a 3x3x3 Monkhorst-Pack k-point mesh. Lattice parameters and atom positions were relaxed until residual forces became less than 0.01 eV/Å. Radial lattice strain and defect formation energy calculations were performed using the 80-atom bixbyite unit cell (space group *Ia*-3) and the PBE+U exchange-correlation functional,[7] where a U value of 4 eV was applied to indium 4d, tin 4d, and cerium 4f states. For a more accurate description of electronic structure, density of states calculations were performed on the 40-atom primitive cell using the HSE06 hybrid functional, with α = 25% exact nonlocal Hartree-Fock exchange.[8,9] A cutoff energy of 450 eV was used for all hybrid functional calculations with lattice parameter and atomic positions fixed to those obtained via PBE+U method. The partial densities of states were projected onto spheres centered around the atom positions with radii of 1.68, 1.57, 1.32 and 0.82 Å for In, Sn, Ce and O, respectively.

Defect formation energies were calculated as a function of electron chemical potential (VBM $\leq \mu_e \leq$ CBM), with CBM determined by the more accurate, hybrid functional band gap, and the chemical potential of the species added and/or removed. The chemical potentials of the atomic species added or removed are limited to a range of obtainable chemical potentials, and they are necessarily related to each other. For the O-poor, metal-rich limiting condition, the chemical potential of the metallic species is set to the energy of atoms in the pure metal, μ_{Metal}, and the chemical potential of oxygen is $\mu_O = {}^1/_3\,\mu_{In_2O_3} - {}^2/_3\,\mu_{In}$. For the O-rich, metal-poor limiting condition, the chemical potential of oxygen is the energy of an oxygen atom in an oxygen molecule, $\mu_O = {}^1/_2\,\mu_{O_2}$ and the chemical potential of the metallic species is given by $\mu_{Metal} = \mu_{Metal\,Oxide} - \mu_O$. The calculated chemical potentials are listed in Table S3 while the $\sum_i n_i\mu_i$ terms used to account for added and removed atoms the calculation of defect formation energy are shown in Table S4.

The correction factor, E_{corr}, in equation 4 in the main text, accounts for finite size effects in charged crystals and includes a potential alignment and image charge correction term. The potential alignment correction (qΔV) accounts for the compensating background charge introduced for charged cell calculations and was determined from the difference in atomic potential of atoms far from the defect in defective and perfect cells.[10] The Makov-Payne correction scheme, as applied by Oba *et al*., was used to account for electrostatic interactions between charged defects.[11,12]

Species (structure)	Energy calculated by DFT (eV)	Formula units per unit cell	Chemical potential (eV)
In_2O_3 (80-atom cubic)	-454.05	16	$\mu_{In2O3,bulk}$= -28.38
SnO_2 (6-atom tetragonal)	-39.38	2	$\mu_{SnO2,bulk}$= -19.69
CeO_2 (12-atom cubic)	-98.64	4	$\mu_{CeO2,bulk}$=-24.66
In metal (2-atom tetragonal)	-4.69	2	$\mu_{In,bulk}$=-2.34
Sn metal (4-atom tetragonal	-15.28	4	$\mu_{Sn,bulk}$=-3.82
Ce metal (FCC)	-17.35	4	$\mu_{Ce,bulk}$=-4.34
O_2 (oxygen molecule)	-8.77	2	μ_O=-4.38

Table S3: Bulk DFT-calculated chemical potentials used for defect energy calculations by Equation 4 in the main text.

Defect	Limit	$\sum_i n_i\mu_i$	Value (eV)
Sn_{In}	O-rich	$\mu_{SnO_2,bulk} - {}^1/_2\,\mu_{In_2O_3,bulk} - {}^1/_2\,\mu_O)$	-3.31
	O-poor	$\mu_{Sn,bulk} - \mu_{In,bulk}$	-1.48
Ce_{In}	O-rich	$\mu_{CeO_2,bulk} - {}^1/_2\,\mu_{In_2O_3,bulk} - {}^1/_2\,\mu_O)$	-8.28
	O-poor	$\mu_{Ce,bulk} - \mu_{In,bulk}$	-2.00
V_O	O-rich	$-\mu_O$	4.38
	O-poor	$-\left[{}^1/_3\,\mu_{In_2O_3,bulk} - {}^2/_3\,\mu_{In}\right]$	7.90

Table S4: $\sum_i n_i\mu_i$ terms used to calculate defect formation energy for different defect species and limiting conditions.

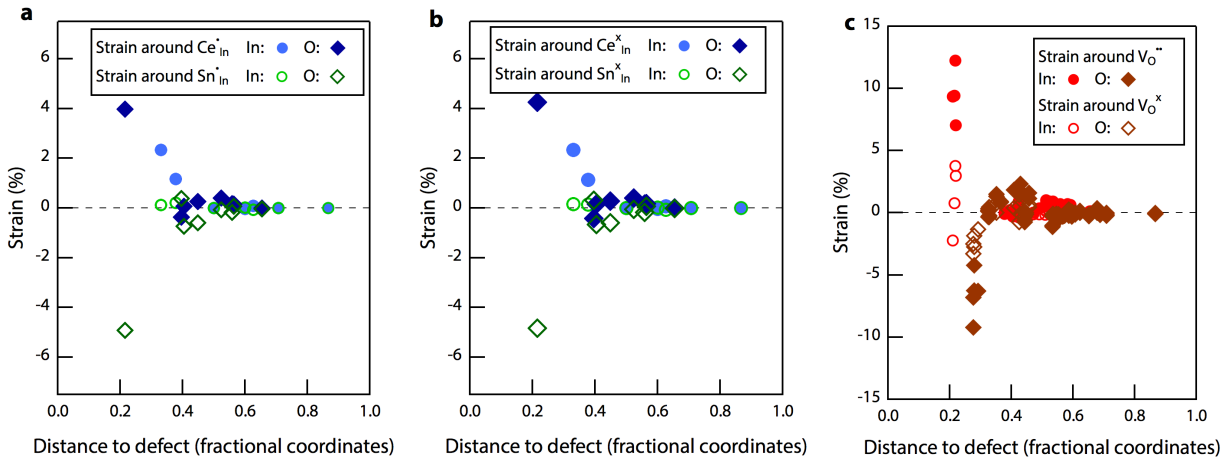

Figure S5: Plots of radial strain from displacement of nearest neighbors (indium atoms denoted by circles, oxygen atoms denoted by diamonds) around a defect as calculated by DFT. a) Strain around ionized Ce (filled blue symbols) and Sn (empty green symbols) dopants. b) Strain around unionized Ce (filled blue symbols) and Sn (empty green symbols). c) Strain around unionized and doubly-ionized oxygen vacancies.

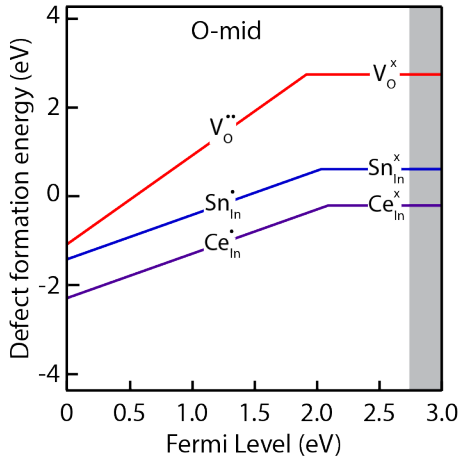

Figure S6: Defect formation energies vs. Fermi level for oxygen vacancies ($V_O^{\bullet\bullet}$, V_O^{x}), substitutional tin dopants ($Sn_{In}^{\bullet}$, Sn_{In}^{x}), and substitutional cerium dopants ($Ce_{In}^{\bullet}$, Ce_{In}^{x}) under conditions with an intermediate chemical potential of oxygen. All chemical potentials in this case are taken as the average chemical potential between the O-poor and O-rich extremes. The valence band maximum is set to 0 eV and the gray shaded region denotes the conduction band edge as determined by the band gap calculated *via* the hybrid functional. The slope of the formation energy vs. Fermi level reflects the stable charge state of the defect at that Fermi level.

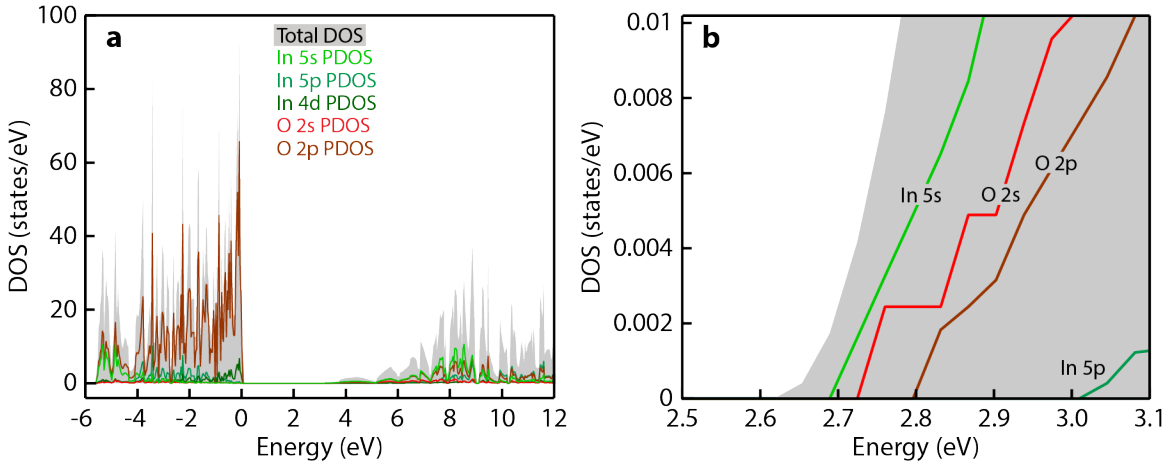

Figure S7: Total and partial density of states calculated by DFT for stoichiometric In_2O_3. The valence band maximum is set to 0 eV. Panel b is a detailed view of the conduction band edge of stoichiometric In_2O_3.

References for Section S5:

1. Hohenberg, P.; Kohn, W. Inhomogeneous Electron Gas. *Phys. Rev.* **1964**, *136*, B864–B871.

2. Kohn, W.; Sham, L. J. Self-Consistent Equations Including Exchange and Correlation Effects. *Phys. Rev.* **1965**, *140*, A1133–A1138.

3. Kresse, G.; Furthmüller, J. Efficiency of Ab-Initio Total Energy Calculations for Metals and Semiconductors Using a Plane-Wave Basis Set. *Comp. Mater. Sci.* **1996**, *6*, 15–50.

4. Kresse, G.; Hafner, J. *Ab Initio* Molecular Dynamics for Liquid Metals. *Phys. Rev. B* **1993**, *47*, 558–561.

5. Kresse, G.; Joubert, D. From Ultrasoft Pseudopotentials to the Projector Augmented-Wave Method. *Phys. Rev. B* **1999**, *59*, 1758–1775.

6. Blöchl, P. E. Projector Augmented-Wave Method. *Phys. Rev. B* **1994**, *50*, 17953–17979.

7. Perdew, J. P.; Burke, K.; Ernzerhof, M. Generalized Gradient Approximation Made Simple. *Phys. Rev. Lett.* **1996**, *77*, 3865–3868.

8. Heyd, J.; Scuseria, G. E.; Ernzerhof, M. Hybrid Functionals Based on a Screened Coulomb Potential. *J. Chem. Phys.* **2003**, *118*, 8207–8215.

9. Krukau, A. V.; Vydrov, O. A.; Izmaylov, A. F.; Scuseria, G. E. Influence of the Exchange Screening Parameter on the Performance of Screened Hybrid Functionals. *J. Chem. Phys.* **2006**, *125*, 224106.

10. Lany, S.; Zunger, A. Accurate Prediction of Defect Properties in Density Functional Supercell Calculations. *Modelling Simul. Mater. Sci. Eng.* **2009**, *17*, 084002.

11. Makov, G.; Payne, M. C. Periodic Boundary Conditions in Ab Initio Calculations. *Phys. Rev. B* **1995**, *51*, 4014–4022.

12. Oba, F.; Togo, A.; Tanaka, I.; Paier, J.; Kresse, G. Defect Energetics in ZnO: A Hybrid Hartree-Fock Density Functional Study. *Phys. Rev. B* **2008**, *77*, 245202.

Section S6: SINS single nanocrystal spectra

Single nanocrystal absorption measurements[1] were performed using a modified atomic force microscope (AFM) at the Advanced Light Source in order to perform synchrotron infrared nano-spectroscopy (SINS).[2] This technique couples light to the near field in the space between an AFM tip and substrate and the scattered light is then collected to measure the complex infrared scattering function of the material that sits beneath the AFM tip with roughly 20nm spatial resolution. Through the extraction of the real and imaginary portion of this function both the particle light absorption and scattering can be ascertained. Lock-in amplification of scattered light was collected at the second harmonic of the AFM tip resonance frequency in order to isolate signal exclusively from the nanocrystal's infrared response. In order to perform SINS on single nanocrystals, dilute dispersions of nanocrystals were spin cast onto gold-coated silicon substrates leading to isolated particles that were sufficiently spaced to eliminate the possibility of inter-particle LSPR coupling. Backgrounds were collected from nearby, empty portions of the substrate to minimize spurious far field contamination of the signal. Single particle scans displayed as absorption represent the imaginary component of the background-subtracted complex scattering function.[3] These scans were performed on several particles to account for particle to particle variations.

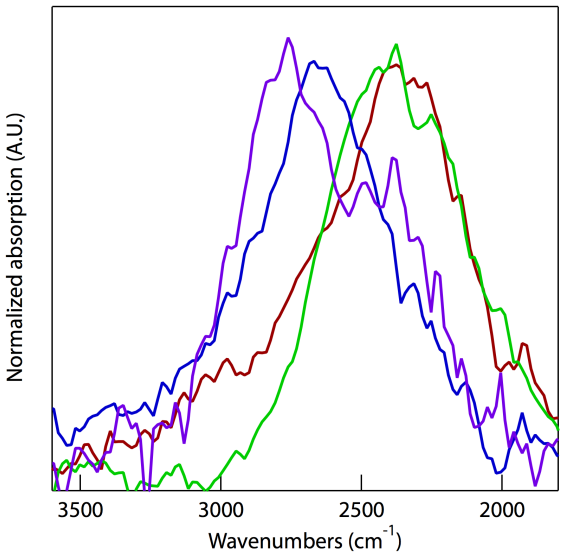

Figure S8: Additional SINS spectra collected from different single Ce:In_2O_3 nanocrystals. The blue spectrum has a FWHM of 479 cm^{-1} at a peak location of 2644 cm^{-1}, corresponding to a quality factor of 5.5.

References for Section S6:

1. Johns, R. W.; Bechtel, H. A.; Runnerstrom, E. L.; Agrawal, A.; Lounis, S. D.; Milliron, D. J. Direct Observation of Narrow Mid-Infrared Plasmon Linewidths of Single Metal Oxide Nanocrystals. *Nat. Commun*. In press.

2. Bechtel, H. A.; Muller, E. A.; Olmon, R. L.; Martin, M. C.; Raschke, M. B. Ultrabroadband Infrared Nanospectroscopic Imaging. *Proc. Natl. Acad. Sci. U.S.A.* **2014**, *111*, 7191–7196.

3. Huth, F.; Govyadinov, A.; Amarie, S.; Nuansing, W.; Keilmann, F.; Hillenbrand, R. Nano-FTIR Absorption Spectroscopy of Molecular Fingerprints at 20 nm Spatial Resolution. *Nano Lett.* **2012**, *12*, 3973–3978.

Section S7: Near field simulations

Frequency-dependent dielectric functions are typically extracted optically *via* the measurement of transmission and reflection of thin film samples. In the case of nanocrystal films, these optical data are usually convoluted with nanocrystal shape/size/interface effects, making the extraction of an accurate dielectric function difficult.

In our work, we use SINS to measure the optical properties of single, isolated nanocrystals to evaluate their dielectric functions. A SINS measurement yields the scattering and absorption characteristics of a coupled tip-nanocrystal-substrate system. To extract a dielectric function from SINS data, one can opt to use analytical methods such as extended finite dipole theory, which has been done previously to calculate the dielectric function of poly(methyl methacrylate) with high spatial resolution.[1] Another option is to use computational methods, which are more flexible. Here, we computationally solve Maxwell's equations for our system of interest, namely the coupled PtSi AFM tip-Ce:In_2O_3 cubic nanocrystal-Au substrate system. Using the COMSOL multiphysics program, the finite element method can be used to discretize each component of the system so that their geometry is accurately represented in solving Maxwell's equations.

The dielectric function of the nanocrystal was determined iteratively. The initial guess for the dielectric function of the cubic nanocrystal was taken from the Drude fit to the ensemble spectrum, while the dielectric functions for PtSi and Au are known. These dielectric functions, along with the finite element method, were then used to simulate the absorption spectrum of the entire coupled structure. Depending on deviations between the simulated spectrum and the experimentally collected SINS spectrum, the plasma frequency and frequency-dependent damping function could be iteratively adjusted to change the dielectric function of the nanocrystal to achieve a match between the experimental and simulated spectra. The flowchart in Figure S9 graphically summarizes this process. After matching the spectra, the dielectric function of the Ce:In_2O_3 nanocrystal was extracted and used to simulate the absorption and near field properties of a single, isolated nanocrystal free of substrate and tip coupling effects.

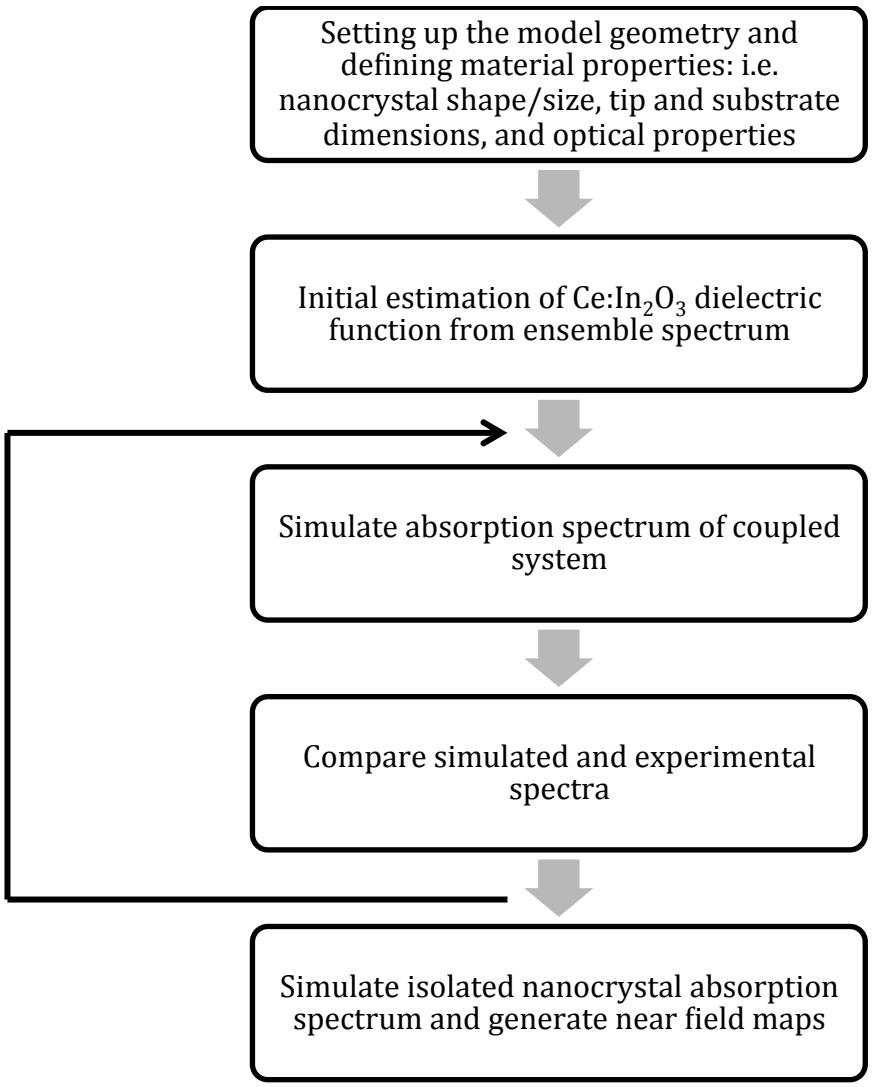

Figure S9: Flowchart depicting process for determining the dielectric function of a Ce:In_2O_3 nanocrystal from an experimental SINS spectrum.

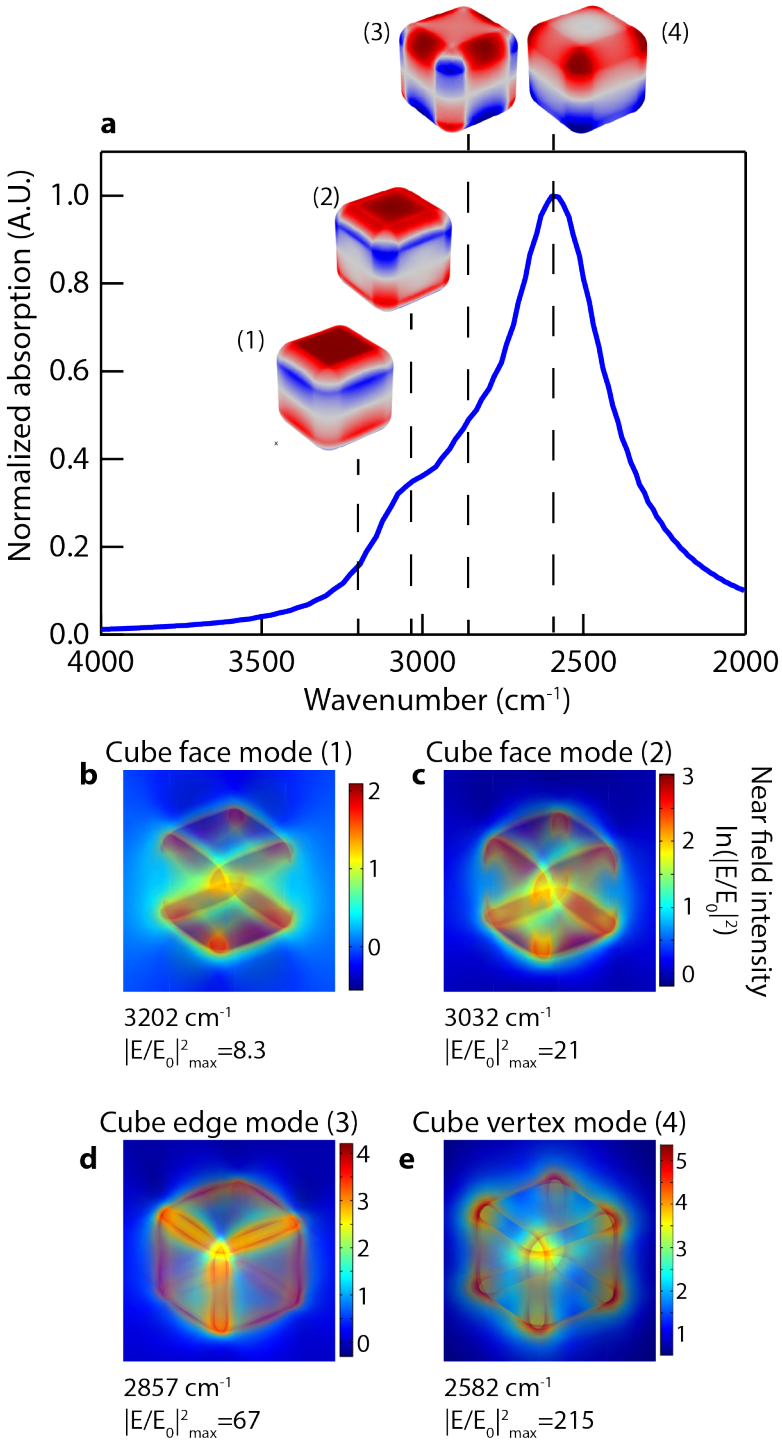

Figure S10: Electric charge density maps (a) and electric near field intensity maps (b-e) of simulated LSPR modes of a Ce:In_2O_3 cubic nanocrystal.

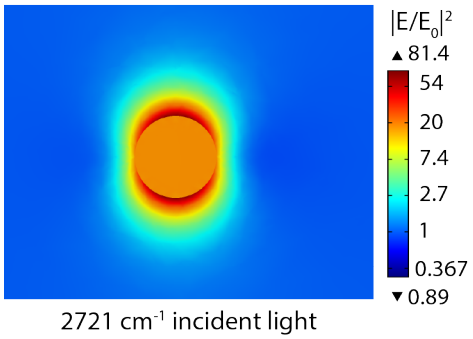

Figure S11: Simulated near field intensity enhancement map of a spherical Ce:In_2O_3 nanocrystal, illuminated at the LSPR peak frequency.

References for Section S7:

1. Govyadinov, A. A.; Amenabar, I.; Huth, F.; Carney, P. S.; Hillenbrand, R. Quantitative Measurement of Local Infrared Absorption and Dielectric Function with Tip-Enhanced Near-Field Microscopy. *J. Phys. Chem. Lett.* **2013**, *4*, 1526–1531.